Linear stability analysis for step meandering instabilities with elastic interactions and Ehrlich-Schwoebel barriers

Dong-Hee Yeon,[1] Pil-Ryung Cha,[2] John S. Lowengrub,[3] Axel Voigt,[4] and K. Thornton[1],*

[1]*Department of Materials Science and Engineering, University of Michigan, Ann Arbor, Michigan 48109, USA*
[2]*School of Advanced Materials Engineering, Kookmin University, Seoul, 136-702 Korea*
[3]*Department of Mathematics, University of California, Irvine, California 92697, USA.*
[4]*Institut für Wissenschaftliches Rechnen, Technische Universität Dresden, Dresden, Germany*

Vicinal surfaces are known to exhibit morphological instabilities during step-flow growth. Through a linear stability analysis of step meandering instabilities, we investigate two effects that are important in many heteroepitaxial systems: elastic monopole-monopole interactions arising from bulk stress and the Ehrlich-Schwoebel (ES) barriers due to the asymmetric adatom incorporation rates. The analysis shows that the effects of the ES barriers increase as the average terrace width increases, whereas the effects of elastic monopole-monopole interactions decrease. The ES barriers favor an in-phase step pattern with a zero phase shift between consecutive steps, while elastic stress favors an out-of-phase pattern with a phase shift of π. However, our analysis shows that the instability growth rate becomes nearly independent of the phase shift when either the ES-barrier effect or the stress effect is large. In particular, for ES-barrier-driven instability, the in-phase step pattern develops only within an intermediate range of terrace widths when bulk stress exists. Similarly, for the elastic-interaction-driven instability, an out-of-phase pattern only forms within a certain range of monopole strength; if the strength is too small, the ES barrier effect dominates, and if it is too large, the peak in the instability growth rate becomes delocalized in the phase shift and no patterns form. This transition between patterned and random step morphologies depends on the monopole strength, but is independent of the terrace width. A phase diagram that describes the regions of the ES-barrier-dominant instability and the elastic-interaction-dominant instability is established, along with the morphological phase diagrams that predict the step configurations as a function of the controlling parameters for the two types of instabilities.

I. INTRODUCTION

Understanding the evolution of steps on a vicinal surface is crucial in many important problems involving surfaces, from the fundamental thermodynamics of surfaces to the fabrication of surface nanostructures. Since modern techniques such as molecular-beam epitaxy (MBE) have enabled nanoscale control during crystal growth, the effort to control the step dynamics has become an important topic in nanoscience research, where the fabrication of nanostructured materials with novel properties is an ultimate goal.

In epitaxial growth, a substrate typically suffers from a miscut, resulting in a surface normal slightly off from a crystallographic direction by what is known as a vicinal angle. The surface is then not completely flat, but rather contains atomic-height steps separated by broad terraces. Under appropriate experimental conditions, a surface may be grown through a regular flow of the steps and growth proceeds monolayer by monolayer [1]. This step-flow growth is essential to the growth of tilted layer superlattices [2,3] and self-organized nanostructures, such as quantum wires [4].

Vicinal surfaces are known to exhibit morphological instabilities during step-flow growth; these instabilities have been observed in many experiments [5–12]. In-phase step meandering caused by the Ehrlich-Schwoebel (ES) barrier on Cu surfaces has been observed [6–8]. Step meandering has

also been observed during evaporation of strained Si surfaces [9–11] and during annealing of strained InGaAs/GaAs pseudomorphic layers [12]. Other factors, such as electric field or impurities, can also cause step meandering. These factors may affect the thermodynamics, the kinetics, or both. Such instabilities can be exploited to achieve self-organized nanostructures on surfaces by creating either a desired structure directly or a template for further growth. In other situations, morphological instabilities of steps are undesirable and must be suppressed. Therefore, extensive fundamental research has been devoted to step dynamics under various growth conditions.

Step-flow growth was first treated quantitatively in the seminal article by Burton, Cabrera, and Frank in 1951 [5,13]. The so-called Burton-Cabrera-Frank (BCF) model describes the evolution of steps by adatom diffusion and incorporation onto the steps. The deposited atoms are first adsorbed to the crystalline surface, and the adsorbed adatoms diffuse along the surface until they are either incorporated into the crystal at the step or desorbed from the surface.

In the years since its introduction, the BCF model has been generalized to include effects of many factors thought to be important in surface step evolution. One such factor is the elastic interactions between the steps. At the steps, there exist surface forces which generate elastic strain energy. These surface forces arise from various sources, such as applied stress, surface stress, epitaxial strain, and thermal stress. In particular, surface stresses and bulk stresses at steps caused by applied stress and/or epitaxial misfit strain engen-

*Electronic address: kthorn@umich.edu

der elastic interactions between steps and thus play an important role in self-organization of surface nanostructures. These interactions can influence the motion of the steps, produce step instabilities [14,15], and generate self-assembled surface patterns [16]. Although much research has been performed to analyze the effects of elastic interactions between the steps on step dynamics [16–25], the kinetics of step instabilities is not fully understood. Stress also affects adatom diffusion on surfaces and at step edges [25,26]. Another important factor influencing step dynamics is that adatoms are preferentially incorporated into the upper step of a terrace. This is due to an asymmetric energy barrier for diffusion across the step, the so-called Ehrlich-Schwoebel barrier, which gives rise to destabilization of straight steps during growth and gathering of steps into groups during evaporation [27–29]. These phenomena are known as step meandering and bunching instabilities, respectively. Bales and Zangwill investigated the ES-barrier-driven morphological instability of the step in the absence of elastic interactions by performing a linear stability analysis [29]. Recently, a morphological stability analysis of a circular island was performed when the ES barrier exist [30].

In this paper, we extend the Bales-Zangwill analysis [29] by including the effects of elastic interactions arising from bulk stress, which are important in many heteroepitaxial systems, and study simultaneously their effects on step meandering instabilities during step-flow growth. Using a linear stability analysis, the step meandering instability is investigated for widely spaced steps and close-packed steps, with a phase shift between consecutive steps. The effects of elastic interactions and the ES barriers are analyzed, the step profiles are predicted, and a phase diagram for the step morphology is established, which describes the regions of the ES-barrier-dominant instability and the elastic-interaction-dominant instability. The paper is organized as follows. In Sec. II, a general introduction to step dynamics is presented. The mathematical descriptions of the ES barriers and elasticity such as force field, displacement field, and elastic interactions are also provided in this section. In Sec. III A, the linear stability analysis for the step meandering instabilities is presented. Section III B contains the discussion of instabilities mediated solely by the ES barriers. We generalize the analysis of Bales and Zangwill by considering the effects of the phase shift. In Sec. III C we discuss the instabilities mediated solely by elastic interactions. Our approach includes intrinsic step-line energy and bulk stress, resulting in a different feature from those of previous theories. We also provide an interpretation of the nonzero growth rate for a perturbation with infinite wavelength. Finally, the competition between these two factors is studied in Sec. III D. In the Appendix, the equilibrium adatom concentration at steps under stress is derived.

II. GENERALIZED STEP DYNAMICS ON SURFACES WITH ELASTIC INTERACTIONS BETWEEN STEPS AND EHRLICH-SCHWOEBEL BARRIERS

Let us consider the step-flow growth without nucleation of islands as described by the BCF model [13]. Let the ada-

tom concentration be $c_m(\vec{r}, t)$, on the mth terrace bounded by the mth step (upper step) and the $(m+1)$th step (lower step). The evolution of the adatom density is described by

$$\frac{\partial c_m}{\partial t} = D\nabla^2 c_m - \frac{c_m - c_{eq}^0}{\tau_s} + F, \qquad (2.1)$$

where D is the surface diffusion coefficient of adatoms, $1/\tau_s$ is the evaporation probability of an adatom per unit time, c_{eq}^0 is the equilibrium concentration of adatoms on a surface, and F is the deposition flux. The first term on the right-hand side of Eq. (2.1) corresponds to the diffusion of adatoms on the crystal surface; the second term and the last term describe evaporation and deposition of adatoms, respectively.

Solving Eq. (2.1) requires mass conservation at steps and with an appropriate choice of boundary conditions at the steps and the computational domain boundary. The mass conservation condition provides the relationship between the normal velocity of the step and the flux of adatom concentration toward the step:

$$\frac{1}{\Omega} v_n^m = D[\ \boldsymbol{\nabla} c_m|_{h_m} - \ \boldsymbol{\nabla} c_{m-1}|_{h_m}] \cdot \hat{\mathbf{n}}_m, \qquad (2.2)$$

where v_n^m is the normal velocity of the mth step, $\hat{\mathbf{n}}_m$ is the unit vector normal to the mth step line, h_m represents the position of the mth step, and Ω is the atomic area of the material. The boundary conditions at the mth step and the $(m+1)$th step are

$$D\,\hat{\mathbf{n}}_m \cdot \boldsymbol{\nabla} c_m|_{h_m} = K_+(\ c_m|_{h_m} - c_{eq}^{h_m}) \qquad (2.3a)$$

and

$$D\,\hat{\mathbf{n}}_{m+1} \cdot \boldsymbol{\nabla} c_m|_{h_{m+1}} = -K_-(\ c_m|_{h_{m+1}} - c_{eq}^{h_{m+1}}), \qquad (2.3b)$$

respectively. K_+ and K_- are the attachment rates of adatoms to the step from the lower terrace and upper terrace, respectively, and $c_m|_{h_m}$ and $c_{eq}^{h_m}$ are the adatom concentration and the local equilibrium concentration of adatoms at the mth step, respectively.

The attachment rates $K_\pm$ depend on the probability that diffusing atoms around the vicinity of steps bond to steps and are also related to the heights of the energy barriers that must be overcome by adatoms during the attachment process. The amount of adatoms incorporated into a step per unit time and length from the upper terrace is $K_+ c_m|_{h_m}$. Because of the detailed balance principle, the number of atoms detaching from a step and moving onto the upper terrace should be equal to $K_+ c_{eq}$. Therefore, the total flux of atoms at the upper side of a step is equal to $-K_+(\ c_m|_{h_m} - c_{eq}^{h_m})$, and this flux should be equal to the normal flux at the upper side step, $-D\hat{\mathbf{n}}_m \cdot \boldsymbol{\nabla} c_m|_{h_m}$.

For $K_\pm \rightarrow \infty$, the equation reduces to the original BCF model, which assumes that the attachment of adatoms to steps is infinitely fast, and thus the concentration of adatoms in the vicinity of each step immediately attains its local equilibrium value on the mth step, $c_{eq}^{h_m}$. However, there exists an additional energy barrier for atoms diffusing from the upper terrace to the step edge, the so-called ES barrier, which causes the attachment rate from the upper terrace to be

smaller than that from lower terrace ($K_- \lesssim K_+$) [27,28,31].

The local equilibrium concentration of adatoms, $c_{eq}^{h_m}$, depends on the chemical potential of adatoms on the mth step. Using a linearized thermodynamics, the local equilibrium concentration of adatoms can be written in terms of the chemical potential of adatoms as

$$c_{eq}^{h_m} = c_{eq}^0 \exp\left(\frac{\Omega}{k_B T}\mu_m\right) \simeq c_{eq}^0\left(1 + \frac{\Omega}{k_B T}\mu_m\right), \quad (2.4)$$

where k_B is the Boltzman constant, T is the temperature, and μ_m is the chemical potential of adatoms on the mth step. In this study, the chemical potential of adatoms on a step is determined by the step-line free energy and the elastic interactions between steps. Thus, the local equilibrium concentration of the mth step is given by

$$c_{eq}^{h_m} \simeq c_{eq}^0\left(1 + \frac{\Omega}{k_B T}\mu_m^\gamma + \frac{\Omega}{k_B T}\mu_m^{el}\right) = c_{eq}^0 + \frac{\Omega c_{eq}^0}{k_B T}\gamma\kappa + \frac{\Omega c_{eq}^0}{k_B T}\mu_m^{el}, \quad (2.5)$$

where γ is the step-line free energy and κ is the local curvature of the step. In this expression, μ_m^γ and μ_m^{el} are the contributions of the step-line energy and the elastic interactions between steps to the chemical potential of adatoms at the mth step on the mth terrace, respectively.

We assume that the elastic interactions between steps are generated by surface forces. Frequently, these surface forces are modeled by two types of forces [16,22]. One is the force monopole, which arises in the presence of bulk stress from the imbalance of stress at a step. The other is the force dipole due to equal and opposite forces from the upper and lower terraces of the step, which are generated by a uniform surface stress. In this study, the force dipole is not considered because it typically generates short-range interactions. For an elastically isotropic system, the surface force field $\mathbf{f}(\mathbf{R})$ at $\mathbf{R}$, generated by a force monopole at $\mathbf{r}^m$ located on the mth step, is given by

$$\mathbf{f}^m(\mathbf{R}) = P\delta(\mathbf{R} - \mathbf{r}^m)\hat{\mathbf{n}}_m, \quad (2.6)$$

where $\mathbf{R}$ and $\mathbf{r}$ are the position vectors on a surface and P is the strength of the force monopole in units of force per unit length.

The relaxation of the elastic field is generally much faster than that of the adatom concentration. Therefore, the elastic field can be obtained by solving the mechanical equilibrium equation

$$\frac{\partial \sigma_{ij}}{\partial x_j} = 0, \quad (2.7)$$

where σ_{ij} is the stress tensor and repeated indices denote summation over the indices. Elastic stress can be obtained using Hook's law, $\sigma_{ij} = \lambda_{ijkl}\epsilon_{kl}$, where λ_{ijkl} is the fourth-order elastic constant tensor which relates the stress tensor σ_{ij} to the infinitesimal strain tensor ϵ_{kl}: $\epsilon_{kl} = (1/2)(\partial u_k/\partial x_l + \partial u_l/\partial x_k)$. For a coordinate where the surface normal vector is parallel with the x_3 axis and the surface is located at $x_3 = 0$, Eq. (2.7) is solved with the following boundary condition which should be satisfied at the surface;

$$\sigma_{ij}(x_3 = 0)k_j = \sigma_{i3}(x_3 = 0) = f_i, \quad (2.8)$$

where $\mathbf{k}$ is the unit vector normal to the surface, $(0,0,1)$.

We compute the solution for the displacement fields using the Green's function formalism [32]. For the isotropic case, the elastic surface Green's function $G_{ij}(\mathbf{R},\mathbf{R}')$ reduces to $G_{ij}(\mathbf{R}-\mathbf{R}')$ [14–16]:

$$G_{ij}(\mathbf{R} - \mathbf{R}') = \frac{1+\sigma}{\pi E}\left[\frac{1-\sigma}{|\mathbf{R} - \mathbf{R}'|}\delta_{ij} + \sigma\frac{(R_i - R_i')(R_j - R_j')}{|\mathbf{R} - \mathbf{R}'|^3}\right], \quad (2.9)$$

where E and σ are Young's modulus and Poisson's ratio, respectively, and δ_{ij} is the Kronecker delta defined as 1 for $i = j$ and 0 otherwise. The displacement field $\mathbf{u}^m(\mathbf{R})$, caused by forces on the mth step, and the elastic interaction energy between the mth and nth steps, $\mathcal{F}_{el}^{mn}$, are obtained using $G_{ij}(\mathbf{R}-\mathbf{R}')$ [32–35]:

$$u_i^m(\mathbf{R}) = \int d\mathbf{R}' G_{ij}(\mathbf{R} - \mathbf{R}')f_j^m(\mathbf{R}') \quad (2.10)$$

and

$$\begin{aligned} \mathcal{F}_{el}^{mn} &= -\int\int ds^m ds^n \int d\mathbf{R} f_i^n(\mathbf{R})u_i^m(\mathbf{R}) \\ &= -\int\int ds^m ds^n\left[\int\int d\mathbf{R}d\mathbf{R}' f_i^n(\mathbf{R})G_{ij}(\mathbf{R} \\ &\quad - \mathbf{R}')f_j^m(\mathbf{R}')\right], \end{aligned} \quad (2.11)$$

respectively, where ds^m is the infinitesimal arclength along the mth step. In Eqs. (2.10) and (2.11), the integrations with respect to $d\mathbf{R}$ and ds^m are performed over the surface and along the mth step, respectively. The total elastic interaction energy $\mathcal{F}_{el}$ can be obtained by summing $\mathcal{F}_{el}^{mn}$ over all pairs of steps. The elastic interactions between different parts of a single step are ignored, but are small as long as the steps are nearly straight. The contribution of elastic interactions to the chemical potential of the mth step is the difference in the elastic interaction energy for an infinitesimal change in the profile of the mth step, $\delta\zeta_m$, and can be obtained from Eq. (2.11):

$$\mu_m^{el} = \sum_{n=-\infty(n\neq m)}^{\infty} \frac{\delta\mathcal{F}_{el}^{mn}}{\delta\zeta_m(x_m)}. \quad (2.12)$$

Thus, the change in the local equilibrium concentration resulting from elastic monopole-monopole interactions can be obtained using an elastic field calculated with the surface elastic Green's function.

III. LINEAR STABILITY ANALYSES FOR STEP MEANDERING INSTABILITY

A. Derivation of the rate of step meandering instabilities

In this section, we present the linear stability analysis for step meandering instabilities against infinitesimal fluctua-

tions on equidistant step positions by generalizing the analysis of Bales and Zangwill [29]. The essential calculations are performed under the quasistatic approximation without desorption for convenience (that is, $\tau_s \to \infty$). Adatom diffusion is generally much faster than step motion, and therefore the time derivative of adatoms, $\partial c/\partial t$, in Eq. (2.1) can be neglected. Thus, Eq. (2.1) becomes

$$D\nabla^2 c_m + F = 0. \tag{3.1}$$

The adatom concentration can then be obtained for a given step distribution, and the step velocity is calculated with Eq. (2.2) using that adatom concentration.

In this study, the x and y axes are set to represent the parallel and normal directions to straight equidistant steps, respectively. For a small perturbation, the positions of the mth and $(m+1)$th steps are $h_m = \ell m + \zeta_m(x)$ and $h_{m+1} = \ell(m+1) + \zeta_{m+1}(x)$, respectively, where ℓ is the average terrace length. Here, ζ_m is a small perturbation to the position of the mth step of the form $A_m e^{iqx}$, where the magnitude of A_m has the order of ϵ.

Within the first order of ϵ, the adatom concentration is written as follows:

$$c_m(x,y) \simeq c_{m0}(y) + c_{m1}(x,y) = c_{m0}(y) + c_{m1y}(y)e^{iqx}, \tag{3.2}$$

where $c_{m1y}(y)$ has the order of ϵ. Solutions of Eq. (3.1), $c_{m0}(y)$ and $c_{m1y}(y)$, are given by

$$c_{m0} = c_{eq}^0 - \frac{F}{2D}(y-m\ell)^2 + A(y-m\ell) + B \tag{3.3a}$$

and

$$c_{m1y} = \alpha_m \sinh[q(y-m\ell)] + \beta_m \cosh[q(y-m\ell)], \tag{3.3b}$$

respectively. In Eqs. (3.3), (A,B) and (α_m, β_m) are determined by the zeroth and first orders of Eqs. (2.3) in ϵ with the local equilibrium concentration of the mth step, $c_{eq}^{h_m}$:

$$
\begin{aligned}
c_{eq}^{h_m} &= c_{eq}^0 + \Gamma(q)\zeta_m(x) \\
&= c_{eq}^0 + \frac{\Omega c_{eq}^0}{k_B T}\left[\gamma q^2 - \frac{4(1-\sigma^2)P^2}{\pi E \ell^2} \sum_{\tilde{n}=1}^{\infty} \frac{\Upsilon(q\ell, \tilde{n}, \varphi)}{\tilde{n}^2} \right]\zeta_m(x),
\end{aligned} \tag{3.4}
$$

where

$$
\begin{aligned}
\Upsilon(q\ell, \tilde{n}, \varphi) &= \int_{-\infty}^{\infty} dt \left[\frac{-t^2+2}{[t^2+1]^{5/2}}[1 - \cos(\tilde{n}\varphi)\cos(q\ell\tilde{n}t)] \right] \\
&\quad + \cos(\tilde{n}\varphi)q\ell\tilde{n}\int_{-\infty}^{\infty} dt \frac{t\sin(q\ell\tilde{n}t)}{[t^2+1]^{3/2}}.
\end{aligned} \tag{3.5}
$$

In Eqs. (3.4) and (3.5), φ is the phase shift between steps. The detailed derivation of $c_{eq}^{h_m}$ is provided in the Appendix. The coefficients in Eq. (3.3) are given by

$$A = \frac{F}{2D}\frac{\ell(2d_2+\ell)}{d_1+d_2+\ell}, \tag{3.6a}$$

$$B = \frac{F}{2D}\frac{d_1(2d_2+\ell)}{d_1+d_2+\ell}, \tag{3.6b}$$

$$
\begin{aligned}
\alpha_m &= A_m \frac{d_2 q \sinh(q\ell) + \cosh(q\ell)}{\mathcal{D}(q,\ell,d_1,d_2)} \\
&\quad \times \left\{ -\Gamma(q) + \frac{F}{2D}\frac{\ell^2 + 2(d_1+d_2)(\ell+d_1)}{d_1+d_2+\ell} \right\} \\
&\quad + A_{m+1}\frac{1}{\mathcal{D}(q,\ell,d_1,d_2)} \\
&\quad \times \left\{ \Gamma(q) + \frac{F}{2D}\frac{\ell^2 + 2(d_1+d_2)(\ell+d_2)}{2D(d_1+d_2+\ell)} \right\},
\end{aligned} \tag{3.6c}
$$

and

$$
\begin{aligned}
\beta_m &= A_m \frac{\sinh(q\ell) + d_2 q \cosh(q\ell)}{\mathcal{D}(q,\ell,d_1,d_2)} \\
&\quad \times \left\{ \Gamma(q) - \frac{F}{2D}\frac{\ell^2 + 2(d_1+d_2)(\ell+d_1)}{d_1+d_2+\ell} \right\} \\
&\quad + A_{m+1}\frac{q d_1}{\mathcal{D}(q,\ell,d_1,d_2)} \\
&\quad \times \left\{ \Gamma(q) + \frac{F}{2D}\frac{\ell^2 + 2(d_1+d_2)(\ell+d_2)}{2D(d_1+d_2+\ell)} \right\},
\end{aligned} \tag{3.6d}
$$

where d_1 and d_2 are defined as D/K_+ and D/K_-, respectively, and $\mathcal{D}(q,\ell,d_1,d_2)$ is defined as

$$\mathcal{D}(q,\ell,d_1,d_2) = (1+q^2 d_1 d_2)\sinh(q\ell) + q(d_1+d_2)\cosh(q\ell). \tag{3.7}$$

With this adatom concentration field, Eq. (2.2) gives the normal velocity of the mth step, v_n^m, within the first order of ϵ: $v_n^m = v_{n0}^m + v_{n1}^m$, where v_{n0}^m and v_{n1}^m are the zeroth- and first-order terms of v_n^m in ϵ, respectively. In order to consider the phase shift between steps, φ, A_m is set to be proportional to $e^{im\varphi}$. Then, v_{n0}^m and v_{n1}^m are given by

$$\frac{v_{n0}^m}{\Omega} = F\ell \tag{3.8a}$$

and

$$
\begin{aligned}
\frac{v_{n1}^m}{\Omega} &= \left\{ \frac{F(d_2-d_1)}{2(d_1+d_2+\ell)}[2(d_1+d_2)\{\cos(\varphi) - \cosh(q\ell) \right. \\
&\quad + q\ell \sinh(q\ell)\} + q\ell^2 \sinh(q\ell)] \\
&\quad - D\Gamma(q)[2\{\cosh(q\ell) - \cos(\varphi)\} + q(d_1+d_2)\sinh(q\ell)] \\
&\quad \left. + iF\frac{\ell+d_1+d_2}{2}\sin(\varphi) \right\}\frac{q}{\mathcal{D}(q,\ell,d_1,d_2)}\zeta_m(x).
\end{aligned} \tag{3.8b}
$$

The initial change in magnitude of the perturbation in time can be regarded as linear:

$$\epsilon = \epsilon_0 e^{rt+i\chi(t)}. \tag{3.9}$$

Here, ϵ_0 is the magnitude of the perturbation at $t=0$ and r represents the growth rate of the meandering instability, where negative r corresponds to decay in the magnitude of the perturbation. In this linear regime, the evolution of the perturbation is given by Eq. (3.9) with

$$r = \Omega q[h(q,\ell,\varphi) + g(q,\ell,\varphi) - q^2 f(q,\ell,\varphi)] \tag{3.10a}$$

and

$$\chi(t) = \frac{\Omega F q(\ell + d_1 + d_2)\sin(\varphi)}{2[(1 + q^2 d_1 d_2)\sinh(q\ell) + q(d_1 + d_2)\cosh(q\ell)]}t. \tag{3.10b}$$

In Eq. (3.10a), $h(q,\ell,\varphi)$, $g(q,\ell,\varphi)$, and $f(q,\ell,\varphi)$ represent the effects of elastic interactions, the ES barriers, and the step-line energy, respectively, and are given by

$$h(q,\ell,\varphi) = \frac{\Omega c^0 D}{k_B T}\left[\frac{4(1-\sigma^2)P^2}{\pi E \ell^2}\sum_{\tilde{n}=1}^{\infty}\frac{\Upsilon(q\ell,\tilde{n},\varphi)}{\tilde{n}^2}\right]\frac{2[1 - \cos(\varphi)\mathrm{sech}(q\ell)] + q(d_1 + d_2)\tanh(q\ell)}{(1 + q^2 d_1 d_2)\tanh(q\ell) + q(d_1 + d_2)}, \tag{3.11a}$$

$$g(q,\ell,\varphi) = \frac{F(d_2 - d_1)}{2(d_1 + d_2 + \ell)}\frac{2(d_1 + d_2)\{\cos(\varphi)\mathrm{sech}(q\ell) - 1 + q\ell\tanh(q\ell)\} + q\ell^2\tanh(q\ell)}{(1 + q^2 d_1 d_2)\tanh(q\ell) + q(d_1 + d_2)}, \tag{3.11b}$$

and

$$f(q,\ell,\varphi) = \frac{\Omega c^0 D \gamma}{k_B T}\frac{2[1 - \cos(\varphi)\mathrm{sech}(q\ell)] + q(d_1 + d_2)\tanh(q\ell)}{(1 + q^2 d_1 d_2)\tanh(q\ell) + q(d_1 + d_2)}. \tag{3.11c}$$

B. Step meandering instability resulting from ES barriers

Without an elastic field [$P=0$ and thus $h(q,\ell,\varphi)=0$], the rate of the meandering instability, r, is determined by the competition between the ES barrier favoring a growth of a perturbation and the step-line energy suppressing it. This meandering instability for $\varphi=0$ was considered by Bales and Zangwill [29]. For a small wave number ($q<q_c$), the effect of the ES barriers is dominant and one would expect to observe spontaneous morphological instabilities. On the other hand, for a large wave number ($q>q_c$), the contribution from the step-line energy is dominant and steps are stabilized. The critical wave number q_c satisfies $r=0$; thus,

$$r = \Omega q_c[g(q_c,\ell,\varphi) - q_c^2 f(q_c,\ell,\varphi)] = 0. \tag{3.12}$$

The critical wave number increases as the magnitude of the deposition flux increases, the ES barrier increases (d_2-d_1 increases), the step-line energy decreases, or the terrace width increases [29]. Thus, for a given value of the ES barrier, the effect of the ES barrier on the instability increases with the terrace width and the flux. Figure 1(a) illustrates the dependence of the critical wave number on the terrace width ℓ for three different values of the flux F. The following parameters are used in calculations throughout this section: $c_0 = 0.01$, $d_1 = 0.0$, $d_2 = 0.5$, $D = 10.0$, $\Omega = 1.0$, and $\tilde{\gamma} = \Omega\gamma/k_B T = 0.5$. Although these material properties are set, the relative magnitude between the effects of the ES barrier and the step-line energy can be controlled by varying the flux. Thus, our results remain general, covering the entire spectrum of the competition between these two factors. Furthermore, in many experiments, controlling the magnitude of the deposition flux is easier than controlling other parameters. Therefore, in Fig. 1(b), we present the critical magnitudes of the deposition flux $F_c(q)$ under the conditions that a fluctuation with a wave number q cannot grow for a deposition flux smaller than $F_c(q)$. When $q_c\ell$ is large enough such that $\tanh(q_c\ell)$ and $\mathrm{sech}(q_c\ell)$ approach 1 and 0, respectively, and if $\ell \gg d_1 + d_2$, then the critical wave number can be approximated as follows:

$$q_c \simeq \frac{-1 + \sqrt{1 + \dfrac{F(d_2 - d_1)(d_1 + d_2)[2(d_1 + d_2) + \ell]}{2\tilde{\gamma}(d_1 + d_2 + \ell)}\ell}}{d_1 + d_2} \tag{3.13a}$$

$$\simeq \frac{-1 + \sqrt{1 + \dfrac{d_2^2 - d_1^2}{2\tilde{\gamma}}F\ell}}{d_1 + d_2}. \tag{3.13b}$$

Equation (3.13b) is plotted together with $q_c(F\ell)$ numerically obtained from Eq. (3.12) for three different values of the flux F in Fig. 1(c), where $F\ell$ is proportional to the average velocity of steps. Equation (3.13) generally provides a good approximation for the critical wave number at high average step velocity.

Next, the effects of the phase shift between steps, φ, are discussed. While the effects of the phase shift φ are diminished in the high-q_c regime (or for large ℓ), these effects are important in the low-q_c regime (or for small ℓ). From Eq. (3.10a), the rate of the meandering instability at $q=0$ is given by
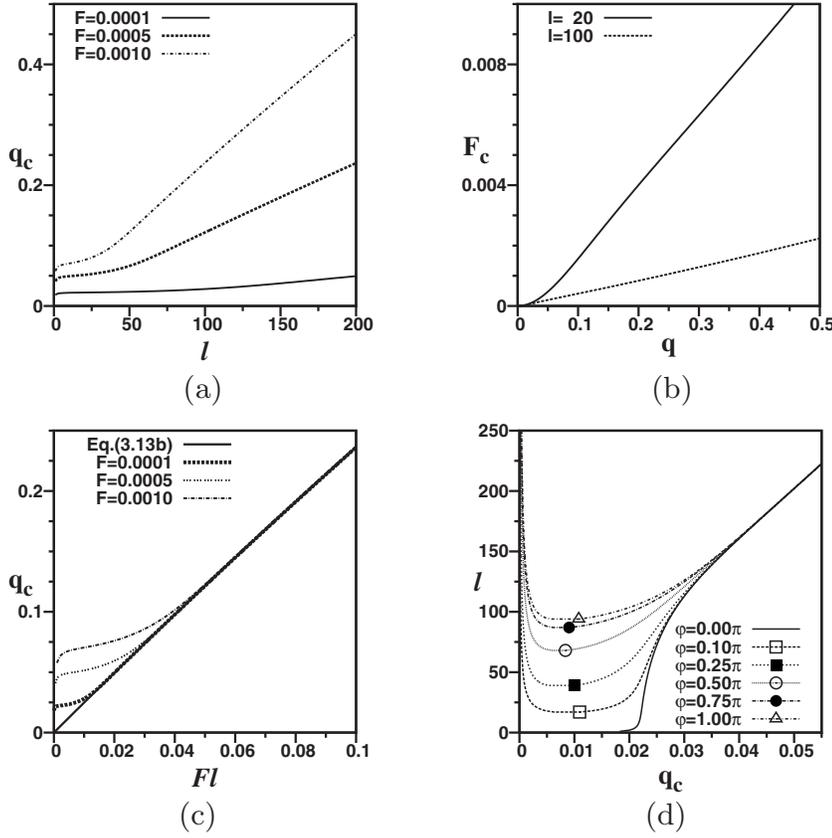
FIG. 1. (a) Plots of the critical wave number q_c vs the terrace width ℓ for different values of the flux F. (b) Plots of the critical deposition flux F_c vs wave number for different terrace widths. (c) Plot of Eq. (3.31b) along with plots of q_c vs $F\ell$ for three different values of F. Note that, although Eq. (3.13b) does not have a linear relationship between q_c and $F\ell$, it behaves linearly with $F\ell$ due to the small range of $(d_2^2 - d_1^2)/(2\tilde{\gamma})(F\ell)$ considered here. (d) Plots of the terrace width ℓ vs the critical wave number q_c for different values of the phase shift φ and $F=0.0001$.

$$r(q=0) = \frac{\Omega F(d_2^2 - d_1^2)(\cos(\varphi)-1)}{(\ell + d_1 + d_2)^2} \leq 0. \quad (3.14)$$

Therefore, a fluctuation with a small wave number and nonzero φ is suppressed not only by the step-line energy, but also by the ES barrier. Figure 1(d) shows the relationships between critical wave numbers and terrace widths for different phase shifts. The perturbations below these curves are stabilized. For example, meandering instabilities for $\ell = 20$ with $\varphi \geq \pi/4$ are suppressed. Figure 1(d) shows clearly that the stable region increases as φ increases.

In Fig. 2, contour plots of the meandering instability rate for different values of the terrace width are presented. The largest critical wave number and the maximum instability rate can be found for $\varphi = 0$, and in-phase modes are most unstable for the ES-barrier-driven step instabilities. As the terrace width increases, effects of the phase shift φ decrease and eventually the critical wave numbers for nonzero φ approach that for $\varphi = 0$, even though the magnitude of the critical wave number increases, as seen in Fig. 1(d).

The evolution of step profiles for different terrace widths as given by the linear analysis are shown in Figs. 3(a) and 3(b). The initial step profiles are established by the superposition of 10 000 instability modes with each wave components having the same amplitude. These 10 000 instability modes are constructed by a combination of 100 different phase shifts uniformly distributed over $[0, \pi]$ and 100 different wavelengths ($\lambda = 2\pi/q$) uniformly distributed over $[\lambda_c^{\max}, 200\lambda_c^{\max}]$ where $\lambda_c^{\max} = 2\pi/q_c^{\max}$ and $q_c^{\max}$ is taken to be the critical wave number for $\varphi = 0.0$. The initial step length is

set as $1000\lambda_c^{\max}$. While the assumption of linearity is not valid when the amplitude of the perturbation becomes large, Figs. 3(a) and 3(b) illustrate the essential pattern exhibited during the linear growth for visualization. For close-packed steps shown in Fig. 3(a), the in-phase instability modes grow faster than other modes and the initial random step profiles with small magnitudes of perturbations become in-phase, resulting in a pattern formation. These in-phase step configurations resulting from the ES barrier have been observed in the growth of steps on Cu surfaces [6–8]. For the widespread steps in Fig. 3(b), the difference among the most unstable growth modes for each phase shift is small and the instability modes corresponding to the in-phase profile grow together with other instability modes. Therefore, the step alignment pattern does not develop. The transition from the patterned in-phase step profile to the nonpatterned step profile occurs as $\tanh(q_c\ell)$ approaches 1, as shown in Fig. 3(c), where the plot of $\tanh(q_c\ell)$ is given together with a plot of q_c vs ℓ for $F = 0.0005$. Figure 3(d) is the phase diagram that divides the regions of the patterned in-phase step alignment from the random step configuration. In the region of the random step configuration, $\tanh(q_c\ell)$ has the value around 1.0 and the line in Fig. 3(d) represents $\tanh(q_c\ell) = 0.999\,999$.

C. Step meandering instability resulting from elastic monopole-monopole interactions between steps

In this section, we consider a special case where the values of d_1 and d_2 are assumed to be 0, and thus the adatom concentration at the steps has its local equilibrium value de-
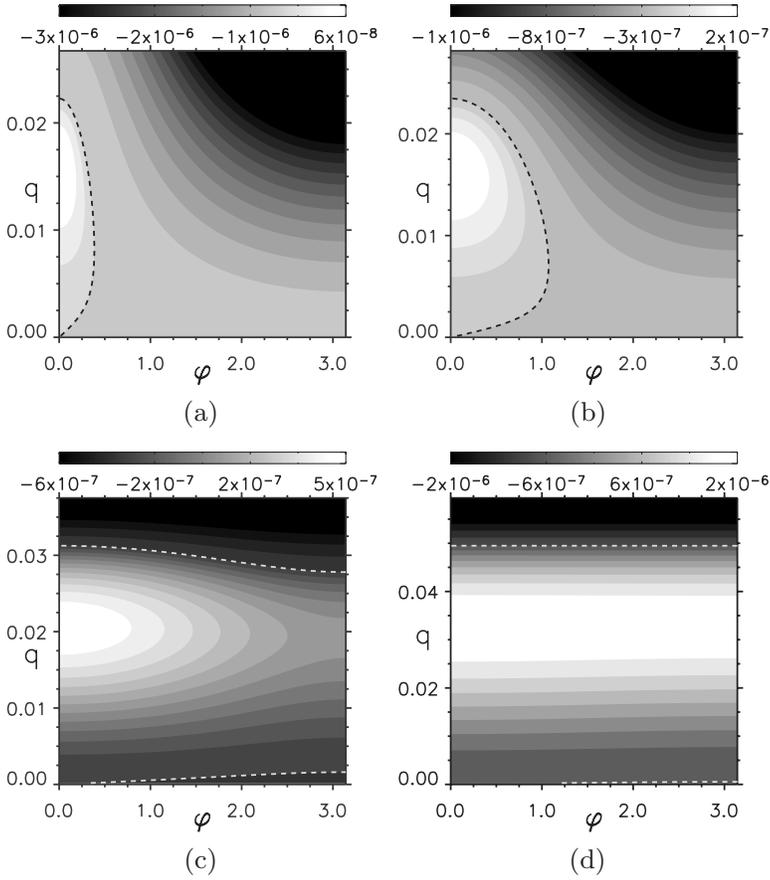
FIG. 2. Contour plots of the growth rate of the meandering instability, r, for different terrace widths with $F=0.0001$. Dashed lines represent the contour line of $r=0$. (a) $\ell=20$, (b) $\ell=50$, (c) $\ell=120$, and (d) $\ell=200$.

termined by the Gibbs-Thomson effect and elastic interactions between steps. Setting $d_1=d_2=0$ (corresponding to $K_\pm \to \infty$) in Eqs. (3.10a), (3.11a), (3.11b), and (3.11c), the rate of the meandering instability is given by

$$r = \Omega \frac{q\tilde{\gamma}}{\ell^2} \frac{2[1-\cos(\varphi)\text{sech}(q\ell)]}{\tanh(q\ell)}$$

$$\times \left[\frac{\tilde{\alpha}P^2}{\tilde{\gamma}} \sum_{\tilde{n}=1}^{\infty} \frac{\Upsilon(q\ell,\tilde{n},\varphi)}{\tilde{n}^2} - (q\ell)^2 \right], \qquad (3.15)$$

where $\tilde{\gamma}$ is defined earlier and $\tilde{\alpha}$ is defined as $(\Omega c_0 D/k_B T) \times [4(1-\sigma^2)/\pi E]$, respectively. Here, we define the characteristic ratio $L=\tilde{\alpha}P^2/\tilde{\gamma}$ that represents the competition between elastic interactions and the step-line energy in a similar manner as was done for a misfitted particle in a matrix [36].

The critical wave number q_c can be obtained by setting r to 0 in Eq. (3.15):

$$L \sum_{\tilde{n}=1}^{\infty} \frac{\Upsilon(q_c\ell,\tilde{n},\varphi)}{\tilde{n}^2} - (q_c\ell)^2 = 0. \qquad (3.16)$$

Solving Eq. (3.16) gives $q_c\ell$ as a function of the strength of monopole, and materials properties such as the step-line energy and elastic properties. The critical wave number of the elastic-interaction-driven step meandering instability is inversely proportional to the terrace width. This is in contrast to the ES-barrier-driven step meandering instability, for

which the critical wave number increases with the terrace width. The plots of the relationships between the critical wave number and the terrace width for different strengths of the force monopole are illustrated in Figs. 4(a) and 4(b). Note that in Fig. 4, φ is set to 0 and the effects of the phase shift are not considered. Throughout this section, $\Omega=1.0$, $\tilde{\gamma} =0.5$, and $\tilde{\alpha}=0.115\,86$ are used and the magnitude of L is controlled by the strength of the force monopole, P. We examine the $P=1.0$ and $P=5.0$ cases. These values translate to L values of 0.23 and 1.16, respectively. Following the analysis of Houchmandzadeh and Misbah [17], we have $P \sim \eta Ea$, where a and η are the atomic spacing and the misfit strain, respectively. Using typical values for 3% misfitted Si ($E=166$ GPa [37], $\sigma=0.217$ [37], and $a=2.346$ Å), L is in the range of 0.1–10 for typical step-line energies $\gamma =10^{-12}-10^{-10}$J/m [11,38]. Therefore, our choice of parameters encompasses experimentally relevant regimes.

For large enough $q_c\ell$ such that $\tanh(q_c\ell)$ approaches 1, $\Upsilon(q_c\ell,\tilde{n},\varphi)$ approaches 2.0, regardless of phase shift φ. The critical wave number in the high $q_c\ell$ regime is thus given by

$$q_c = \sqrt{\frac{\pi^2 L}{3}} \frac{1}{\ell} = \sqrt{\frac{4\pi(1-\sigma^2)}{3E\gamma}} \frac{P}{\ell}. \qquad (3.17)$$

In Fig. 4(b), $q_c\sqrt{3/(\pi^2 L)}$ is plotted against $1/\ell$ for different strengths of force monopole. The line given by Eq. (3.17), whose slope is equal to 1.0, is also included in Fig. 4(b). While each line shows linear behavior with $1/\ell$ for all P, only the lines with large P obey Eq. (3.17). The slopes of the
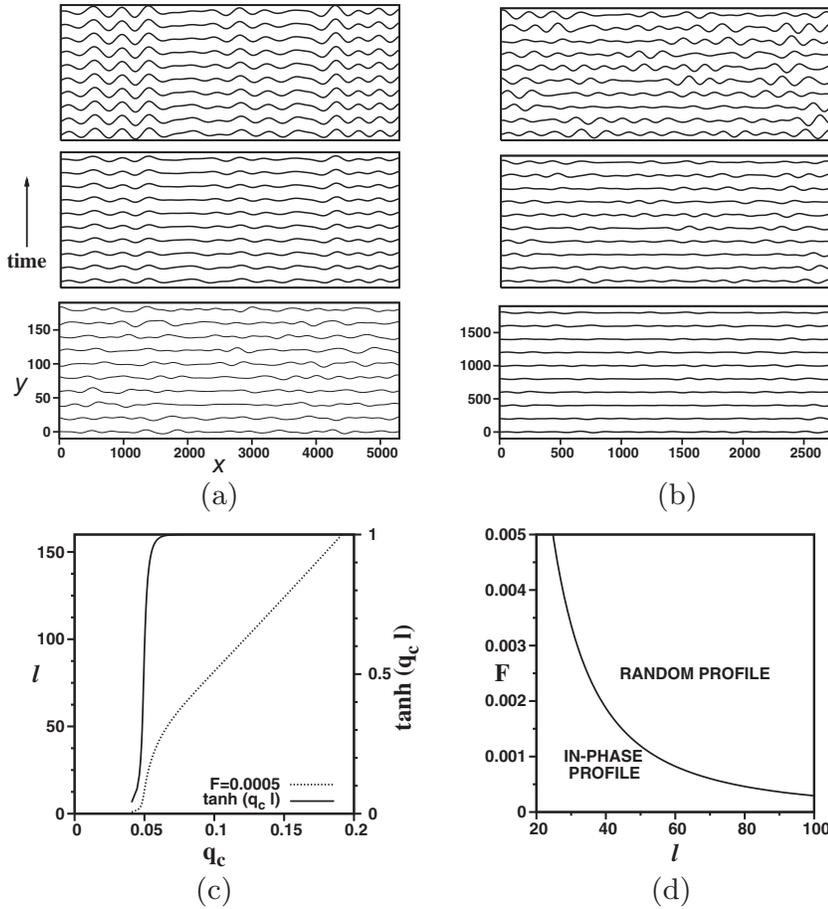
FIG. 3. (a) Evolution of step profiles for terrace width, $\ell=20$ with $F=0.0001$. The figures are captured at $t=0.0$, $t=2.0t_0$, and $t=3.0t_0$, where t_0 is 3.339×10^8. (b) Evolution of step profiles for the terrace width, $\ell=200$ with $F=0.0001$. The figures are captured at $t=0.0$, $t=2.5t_0$, and $t=3.5t_0$, where t_0 is 2.762×10^6. (c) Plot of ℓ vs q_c along with $\tanh(q_c\ell)$ for $F=0.0005$. (d) Morphological phase diagram dividing the regions of the patterned in-phase step alignment and the random step configuration.

lines for small P are smaller than the values suggested by Eq. (3.17) and must be calculated numerically. Figure 4(c) shows the critical strengths of the force monopole, $P_c(q)$, for a given terrace width, defined as the strength of the force monopole below which step instabilities are suppressed at wave number q.

The effects of the phase shift on instabilities driven by monopole-monopole interactions are important in the small-$q_c\ell$ regime and diminish as $q_c\ell$ increases. The variation of q_c with ℓ for different values of φ is shown in Fig. 5. The critical wave number for a given ℓ is smallest at $\varphi=0$ and largest at $\varphi=\pi$ for the elastic-interaction-driven instability, but the difference between these values decreases as the strength of the force monopole increases. Therefore, the fastest growing mode occurs with out-of-phase alignment for the elastic-interaction-driven step instabilities when P is small, but the growth rate becomes insensitive to the phase shift when P is large. Therefore, no pattern is expected to form when there is sufficiently large bulk stress. Nonpatterned step morphology has been observed during annealing of
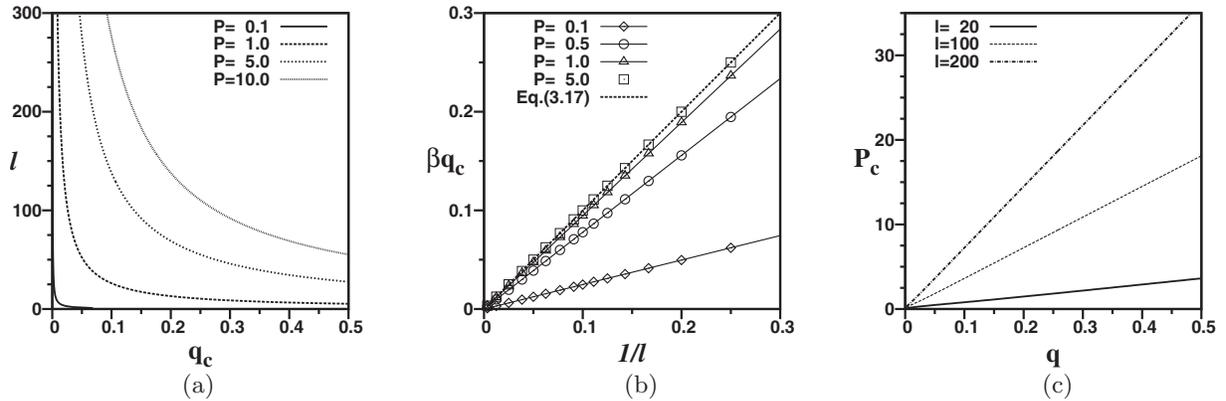

FIG. 4. (a) Plots of terrace width ℓ vs the critical wave number q_c for different strengths of the force monopole, $P=0.1$, 1.0, 5.0, and 10.0. The region below the curves is where the step meandering instabilities occur. (b) Plots of βq_c vs $1/\ell$ for $P=0.1$, 0.5, 1.0, and 5.0, where $\beta=\sqrt{3/(\pi^2 L)}$. (c) Plots of the critical strength of the force monopole, P_c, vs the wave number for different terrace widths.
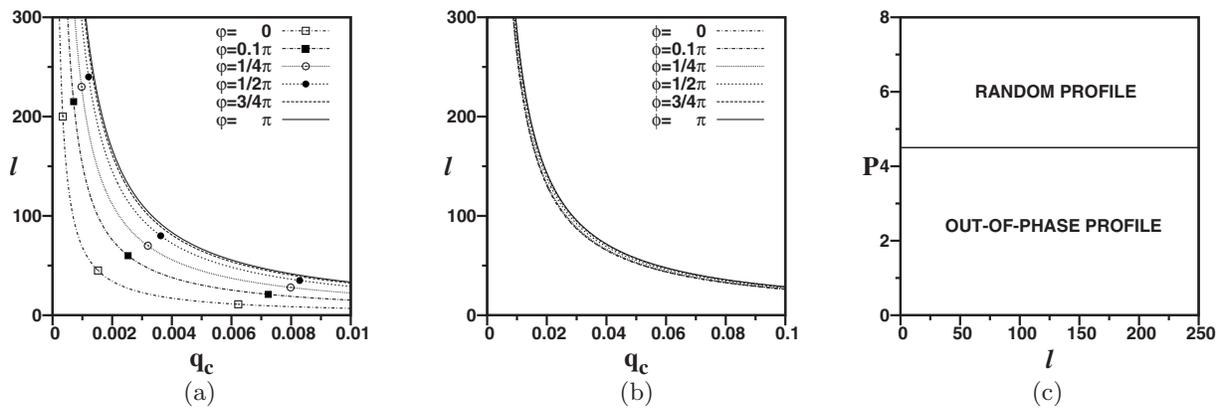
FIG. 5. Plots of the terrace width ℓ vs the critical wave number q_c for various values of phase shift φ (φ=0, 0.1π, 1/4π, 1/2π, 3/4π, and π) for a given strength of the force monopole P. (a) P=0.1 and (b) P=1.0 (c) Morphological phase diagram dividing the regions of the patterned out-of-phase step alignment and the random step configuration.

stressed surfaces, where the effects of the ES barrier can be excluded [12]. Note that the functional form of the growth rate of meandering instabilities is independent of the terrace width and is determined by the properties of the material, such as the elastic constants and step-line energy, as well as the strength of the force monopole, which depends also on the magnitude of the applied stress. Only its magnitude depends on the terrace width. We present the morphological phase diagram in Fig. 5(c), which divides the regions of the patterned out-of-phase step alignment and the random step configuration. It shows that the expected step morphology is independent of the terrace width. The line in Fig. 5(c) represents $\tanh(q_c\ell)$=0.999 999.

In order to investigate the most unstable mode resulting from elastic monopole-monopole interactions, the rate of meandering instabilities for different monopole strengths (P=1.0 and P=5.0) and different terrace widths (ℓ=50 and ℓ=250) is given as a function of q and φ in Fig. 6. Figure 6 shows that the functional shape of the instability rate is sensitive to the strength of the force monopole, but is independent of the average terrace width. The most unstable mode is located around q=0 for small P but its location moves to nonzero q as P increases. Note that the instability rates for $\varphi \neq 0$ approach nonzero values as $q \rightarrow 0$ although our linear stability analysis does not include the instability for q=0 (see
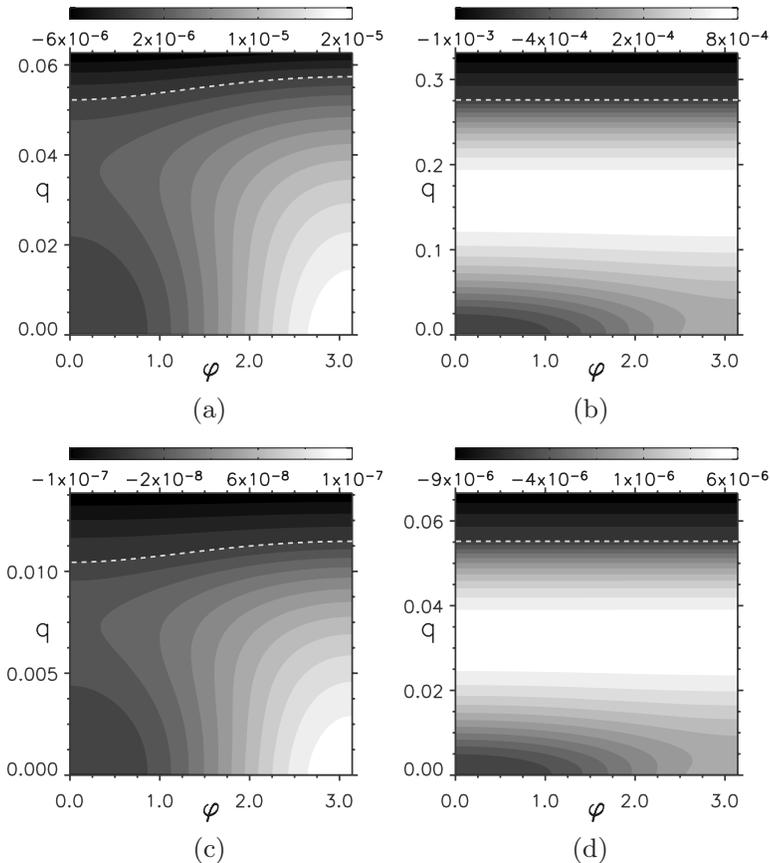

FIG. 6. Contour plots of the growth rate r vs the wave number q and phase shift φ for different monopole strengths and terrace widths. For small monopole strength [(a) and (c)], the most unstable mode is located around φ=π and out-of-phase step alignment is expected. (a) P=1.0 and ℓ=50, (b) P=5.0 and ℓ=50, (c) P=1.0 and ℓ=250, and (d) P=5.0 and ℓ=250.
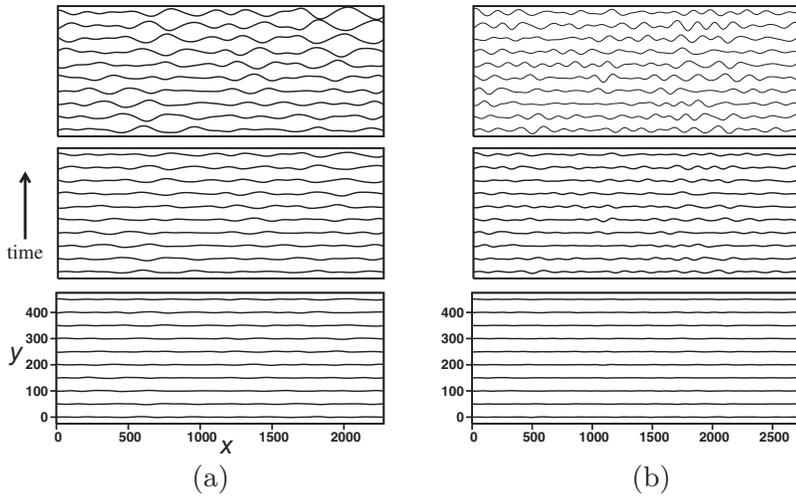
FIG. 7. (a) Evolution of the step profiles with the strength of force monopole, $P=1.0$. The figures are captured at $t=0.0$, $t=3.0t_0$, and $t=5.0t_0$, where t_0 is 2.994×10^5. (b) Evolution of step profiles against time for the strength of the force monopole, $P=5.0$. The figures are captured at $t=0.0$, $t=4.0t_0$, and $t=6.0t_0$, where t_0 is 640.7.

the Appendix). From Eq. (3.15), the instability rate for $\varphi = \pi$ as $q \rightarrow 0$ is given by as follows:

$$\lim_{q \rightarrow 0} r = \Omega \frac{2\pi^2 \tilde{\alpha} P^2}{\ell^2}. \qquad (3.18)$$

Thus, the instability rates as $q \rightarrow 0$ are determined not by step-line energy $\tilde{\gamma}$, but by the elastic constant $\tilde{\alpha}$, the strength of the force monopole, P, and the terrace width ℓ.

Similar behavior of step meandering instabilities with a phase shift has been investigated by Leonard and Tersoff [24]. The main difference between their approach and ours lies in the treatment of the step-line energy. They considered the step-line energy resulting from the elastic self-interaction. In contrast, we treat the step-line energy to be intrinsic, present even in the absence of elastic stress, following Bales and Zangwill [29]. Leonard and Tersoff's result has a qualitative feature of the instability rates similar to that in Fig. 6. However, in their case the main factor that determines the functional form of the rate of the meandering instability is not the strength of the force monopole, but rather the terrace width for given elastic properties.

Furthermore, Leonard and Tersoff interpreted the instability at $(q, \varphi) = (0, \pi)$ for small terrace widths as the step bunching instability and thus concluded that meandering instabilities would occur for steps with large terrace widths, while step bunching instabilities would occur for close-packed steps. However, to examine whether a step bunching instability occurs, one must perturb the terrace widths. Since the basic assumption of our analysis is that the spacing between the average location of neighboring steps remains constant throughout the evolution, a bunching instability, wherein the terrace width must change, cannot be modeled. To consider step bunching and step meandering simultaneously, we must apply sinusoidal perturbations on nonequidistant, straight steps. In this study, due to the difficulties of obtaining analytic solutions for the elastic field with both bunching and meandering perturbations, we only consider meandering instabilities, as in Ref. [24]. Therefore, no information about a bunching instability can be obtained from the analysis, although it is expected to occur from previous

analyses [21,39]. In our interpretation, the fastest growing unstable mode at $\varphi = \pi$ and $q \rightarrow 0$ observed for small P corresponds to that of infinite wavelength. More intuitively, this means that the fastest growing mode for a given domain (physical or computational) may be the one that just fits the domain. In practice, however, only modes with nonzero amplitude can grow, and the fastest growing mode will be the one that has the longest wavelength with sufficiently large initial amplitude. This implies that the evolution of the step morphology is highly sensitive to the initial condition. The growth of long-wave modes can occur not only for steps with large separation, but also for close-packed steps when P is small, in the absence of ES barriers as assumed in this section.

This result is similar to the linear stability analysis of the Allen-Cahn equation, in which the fastest growth mode has $q \rightarrow 0$ [40]. In that case, the result stems from the fact that phase transformation of nonconserved order parameter does not require mass transport. In our case, however, mass transport must take place, and therefore the origin of the result is quite different. Note that we (and Leonard and Tersoff) obtain a nonzero growth rate as $q \rightarrow 0$ when two consecutive steps are out of phase. In such a case, mass transport perpendicular to the average step position dominates transport along the average step position. Therefore, increasing the length scale along the average step position does not hinder the growth of the perturbation. In this case, the instability growth rate at $q \rightarrow 0$ is nonzero and can be maximum. On the other hand, for in-phase steps, mass transport must occur along the parallel direction, and therefore the growth rate is zero at $q=0$ since mass transport takes an infinite amount of time as the wavelength approaches infinity.

The evolution of step profiles for $P=1.0$ and $P=5.0$ is presented in Fig. 7. The initial step profiles are established in the same manner as in Sec. III B, except that q_c^{max} is chosen as the critical wave number for $\varphi=\pi$. For $P=1.0$, the instability modes corresponding to out-of-phase alignment grow faster than other modes, and the initially nearly straight step profiles with small random perturbations become dominated by the out-of-phase ordering. We set the largest wavelength of perturbation to be $1/5$ of the computational domain to highlight the out-of-phase alignment. For $P=5.0$, the growth
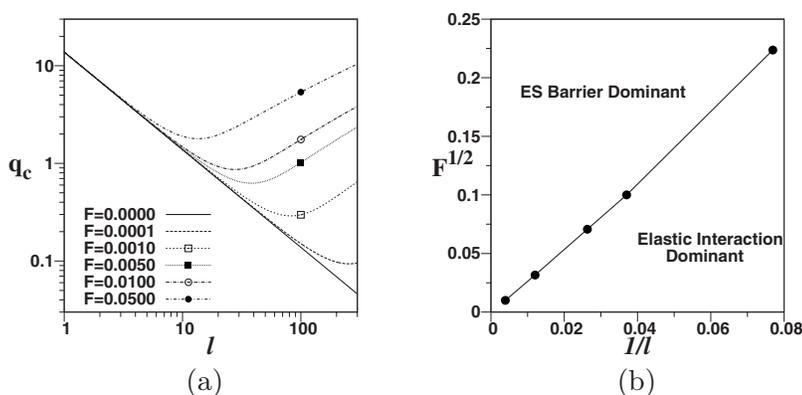
FIG. 8. (a) Log-log plots of the critical wave number vs terrace width ℓ for different magnitudes of the deposition flux. The input parameters used in the calculation are $\Omega=1.0$, $c_0=0.01$, $d_1=0.0$, $d_2=0.5$, $D=10.0$, $\Omega\gamma/k_BT=0.5$, $\varphi=0.0$, $(\Omega/k_BT)[4(1-\sigma^2)/\pi E]=1.158$, and $P=5.0$. (b) A phase diagram of step meandering instabilities.

rates of the most unstable modes for each φ value become nearly independent of φ. Therefore, no particular pattern forms during step evolution.

Finally, we will briefly discuss the effects of force dipoles neglected in this study. Whereas elastic monopole-monopole interactions produce attraction between steps, elastic dipole-dipole interactions generate repulsion between steps and alter the behavior of meandering instabilities [17,18,25]. Dipole-dipole interactions are especially important in homoepitaxial systems, where bulk stress is negligible. On the other hand, since monopole-monopole interactions are long ranged and dipole-dipole interactions are short ranged, the dipole-dipole interactions are expected to be negligible when bulk stress exists and the terrace width is sufficiently large. Therefore, our results remain valid in this regime. However, when the effect of dipole-dipole interactions is large, the most unstable mode will have in-phase alignment [17,18]. Consequently, the step morphology will be determined by how the two effects compete, and thus a full analysis that includes both monopole-monopole and dipole-dipole interactions must be performed to study this regime.

D. Step meandering instabilities when the ES barrier and elastic monopole-monopole interactions coexist

If the elastic monopole-monopole interactions and the ES barriers are simultaneously important, both of these factors play a role in step meandering instabilities against the step-line energy. However, their manner of contribution to the instabilities is different. As the terrace width increases, the effects of the ES barriers increase, whereas those of elastic monopole-monopole interactions decrease. Figure 8(a) shows the relationships among critical wave numbers, terrace widths, and magnitudes of the deposition flux for the given material properties. When the terrace width is large, the ES barriers play a dominant role in the step meandering instabilities, and thus the critical wave number increases with the terrace width. For close-packed steps, the effects of elastic interactions dominate and the critical wave number decreases with the terrace width. If the elastic-interaction-dominant regime is defined as the regime where the critical wave number decreases with the terrace width, the elastic-interaction-dominant regime and the ES-barrier-dominant regime can be divided as shown in Fig. 8(b). In this figure, the line represents the terrace width at the minimum growth rate

for a given flux. As a result of the choice of $P(=5.0)$ in Fig. 8, the effect of the phase shift is not observed. This is because the strength of the force monopole is large enough so that the effects of the phase shift disappear [e.g., Fig. 5(b)]. When the terrace width is large, the phase shift does not affect the instability because it is driven by the ES barrier.

When the strength of the force monopole is small, on the other hand, the effects of the phase shift are observed for close-packed steps. Figure 9 shows the instability rates for different values of the terrace width when the ES barriers and elastic interactions coexist for the case of $P=1.0$. The characteristics of the ES-barrier-driven instability can be observed for large terrace widths [$\ell=100$ in Fig. 9(c) and $\ell=150$ in Fig. 9(d)], where the critical wave numbers become independent of φ. Clearly, the functional shape of the meandering instability rate r in the (q,φ) plane depends on the terrace width ℓ. This is different from the purely elastic-interaction-driven instability. The dependence of the critical wave number on the phase shift stemming from the ES barrier is not observed because the small-ℓ regime is dominated by elastic monopole-monopole interactions.

Figure 10 shows the instability rates for $P=0.1$. The effects of phase shift stemming from the ES barriers and elastic interactions coexist for a small terrace width. According to Fig. 10(a), elastic interactions are dominant and the out-of-phase step profile is expected. When the terrace width increases to $\ell=50$, two peaks in r appear as the contribution of the ES barriers to the step meandering instability increases. One peak occurs at $\varphi=\pi$ and small wave numbers due to elastic interactions, while another peak develops at $\varphi=0$ and large wave numbers due to the ES barriers [cf. Fig. 10(b)]. Therefore, these two fast growth modes grow simultaneously and the surface will develop no step patterns. For $\ell=100$ [Fig. 10(c)], the effects of the ES barriers are dominant over elastic interactions and the surface has the in-phase pattern. Finally, for a large terrace width of $\ell=150$ [Fig. 10(d)], the maximum rate becomes nearly independent of φ and thus the steps develop no patterns.

IV. SUMMARY

In this paper, the effects of elastic monopole-monopole interactions and the Ehrlich-Schwoebel barriers on step meandering instabilities during step-flow growth were investigated by a linear stability analysis. We found that the effects
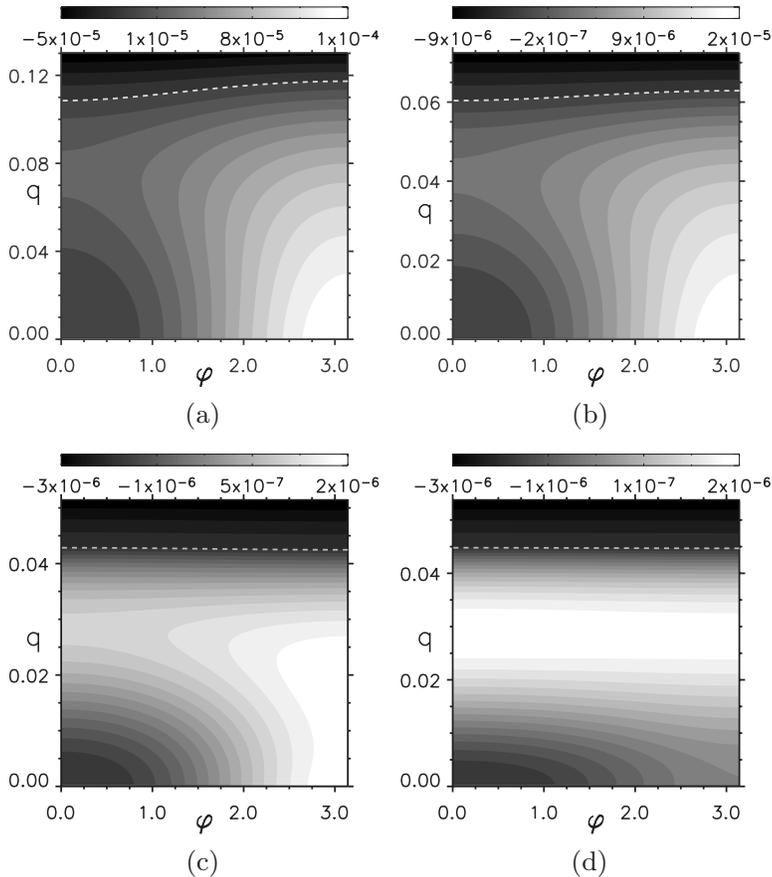
FIG. 9. Contour plots of the growth rate of the meandering instability for $P=1.0$. The input parameters used in the calculation are $\Omega=1.0$, $c_0=0.01$, $d_1=0.0$, $d_2=0.5$, $D=10.0$, $\Omega\gamma/k_BT=0.5$, $\varphi=0.0$, $(\Omega/k_BT)[4(1-\sigma^2)/\pi E]=1.158$, and $F=0.0001$. (a) $\ell=25$, (b) $\ell=50$, (c) $\ell=100$, and (d) $\ell=150$.

of the ES barriers increase with the average terrace width, whereas those of elastic monopole-monopole interactions decrease. The most unstable mode for the step meandering instability mediated by the ES barrier has in-phase step alignment, while that driven by elastic monopole-monopole interactions has out-of-phase step alignment. In the former, where in-phase step alignment is favored, the instability growth rate becomes insensitive to the phase shift as the terrace width increases (and thus the ES barrier effect increases). Therefore, the in-phase patterns predicted by Bales and Zangwill are expected to form only when the terrace width is sufficiently large such that the ES barrier effects dominate the elastic interactions but is sufficiently small so that the instability growth rate has a distinct peak at zero phase shift. Similarly, we find that out-of-phase patterns with a phase shift of π, expected from elastic monopole-monopole interactions, form only in a certain range of monopole strength. If the strength is too small, the ES barrier effect dominates, and if it is too large, the peak in the instability growth rate becomes delocalized in the phase shift. We investigated two values of the force monopole strength in detail, which exhibit very different step morphologies. We also show that the dependence of the instability rate on the wave number and the phase shift is sensitive to the strength of the force monopole, but is independent of the average terrace width. For the case where the ES barrier and elastic interaction effects compete, a phase diagram was established to describe the regions of the ES-barrier-dominant instability and the elastic-interaction-dominant instability.

APPENDIX: EQUILIBRIUM ADATOM CONCENTRATION AT A CORRUGATED STEP UNDER STRESS

In this section, we will derive the expression for the equilibrium concentration at a corrugated step when a force monopole with strength P is located at the steps.

For a small perturbation on equidistant steps, the position of the mth step, $\mathbf{r}^m$, and the unit normal vector $\hat{\mathbf{n}}(\mathbf{r}^m)$ are given by

$$\mathbf{r}^m = x_m\hat{\mathbf{i}} + h_m(x_m)\hat{\mathbf{j}} = x_m\hat{\mathbf{i}} + [\ell m + \zeta_m(x_m)]\hat{\mathbf{j}} \qquad \text{(A1)}$$
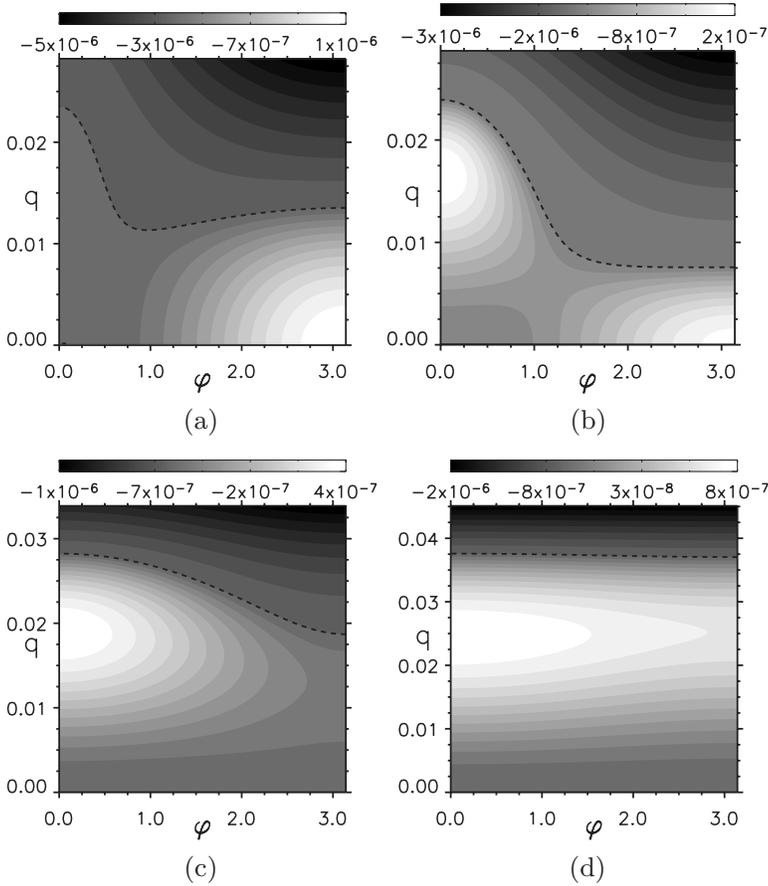
and

FIG. 10. Contour plots of the growth rate of the meandering instability for $P=0.1$. The input parameters used in the calculation are same with those in Fig. 9. (a) $\ell=25$, (b) $\ell=50$, (c) $\ell=100$, and (d) $\ell=150$.

$$\hat{\mathbf{n}}^m(\vec{r}_m) = \frac{1}{\sqrt{1+(\zeta_m')^2}}(-\zeta_m'\hat{\mathbf{i}}+\hat{\mathbf{j}}), \qquad (A2)$$

respectively, where $\zeta_m'=\partial\zeta_m(x_m)/\partial x_m$. Here, ℓ is the average length of the terrace and the magnitude of the perturbation $\zeta_m(x_m)$ is of the order of ϵ.

The elastic interaction between *two point forces* located at $\mathbf{r}^m$ and $\mathbf{r}^n$ is given by

$$\mathcal{E}(\mathbf{r}^m,\mathbf{r}^n) = -\int d\mathbf{R}f_i^m(\mathbf{R})u_i^n(\mathbf{R}) = -\int d\mathbf{R}f_i^n(\mathbf{R})u_i^m(\mathbf{R})$$

$$= -\int\int d\mathbf{R}d\mathbf{R}'f_i^m(\mathbf{R})G_{ij}(\mathbf{R},\mathbf{R}')f_j^n(\mathbf{R}')$$

$$= -\frac{(1+\sigma)P^2}{\pi E}\frac{1}{\sqrt{1+\zeta_m'^2}}\frac{1}{\sqrt{1+\zeta_n'^2}}\left[\frac{1-\sigma}{r}(\zeta_m'\zeta_n'+1)\right.$$

$$\left. +\frac{\sigma}{r^3}\{r_1^2\zeta_m'\zeta_n'-r_1r_2(\zeta_m'+\zeta_n')+r_2^2\}\right], \qquad (A3)$$

where $r_1=x_m-x_n$, $r_2=\ell(m-n)+\zeta_m(x_m)-\zeta_n(x_n)$, and $r=\sqrt{r_1^2+r_2^2}$. The force field $\mathbf{f}^m$, displacement field $\mathbf{u}^m$, and Green's function $G_{ij}(\mathbf{R},\mathbf{R}')$ are introduced in Eqs. (2.6), (2.9), and (2.10).

The elastic monopole-monopole interaction energy between the mth step and nth steps, $\mathcal{F}_{\mathrm{el}}^{mn}$, is given by the integration of $\mathcal{E}(\mathbf{r}^m,\mathbf{r}^n)$ along the mth and nth steps. For a small

perturbation of $\zeta_m(x_m)$ and $\zeta_n(x_n)$, $\mathcal{F}_{\mathrm{el}}^{mn}$ within the second order of ϵ is given by

$$\mathcal{F}_{\mathrm{el}}^{mn} = \int\int ds_m ds_n \mathcal{E}(\mathbf{r}^m,\mathbf{r}^n)$$

$$\simeq -\frac{(1-\sigma^2)P^2}{\pi E}\int_{-\infty}^{\infty}\int_{-\infty}^{\infty}dx_m dx_n\left[\frac{1}{r_0}-\frac{\ell(m-n)}{r_0^3}\right.$$

$$\times(\zeta_m-\zeta_n)+\frac{1}{2}\frac{1-(x_m-x_n)^2+2\ell^2(m-n)^2}{r_0^5}$$

$$\left.\times(\zeta_m-\zeta_n)^2+\frac{1}{r_0}\zeta_m'\zeta_n'\right], \qquad (A4)$$

using

$$\frac{1}{r} = \frac{1}{r_0}-\frac{\ell(m-n)}{r_0^3}(\zeta_m-\zeta_n)$$

$$+\frac{1}{2}\frac{2\ell^2(m-n)^2-(x_m^2-x_n^2)}{r_0^5}(\zeta_m-\zeta_n)^2+O(\epsilon^3),$$

where ds_m is the infinitesimal arclength of the mth step and $r_0=\sqrt{(x_m-x_n)^2+\ell^2(m-n)^2}$.

In order to obtain the chemical potential of an adatom at the mth step, $\delta\mathcal{F}_{\mathrm{el}}^{mn}/\delta\zeta_m(x)$ should be calculated. Applying the variation to both sides of Eq. (A4) gives

$$\delta\mathcal{F}_{\text{el}}^{mn} = -\frac{(1-\sigma^2)P^2}{\pi E}\int_{-\infty}^{\infty}\int_{-\infty}^{\infty}dx_m dx_n\left[-\frac{\ell(m-n)}{r_0^3}\right.$$

$$\times[\delta\zeta_m(x_m) - \delta\zeta_n(x_n)] + \frac{-(x_m-x_n)^2 + 2\ell^2(m-n)^2}{r_0^5}$$

$$\times[\zeta_m(x_m) - \zeta_n(x_n)][\delta\zeta_m(x_m) - \delta\zeta_n(x_n)]$$

$$\left. + \frac{x_m - x_n}{r_0^3}\frac{\partial\zeta_m(x_m)}{\partial x_m}\delta\zeta_n(x_n) - \frac{\partial\zeta_n(x_n)}{\partial x_n}\zeta_m(x_m)\right].\quad \text{(A5)}$$

Here, we will consider the sinusoidal fluctuation with its magnitude ϵ and its wave number q, where the phase difference with respect to the nearest step is φ. Now, we set $\zeta_m(x_m)$ and $\zeta_n(x_n)$ to $\epsilon\cos(qx_m + m\varphi)$ and $\epsilon\cos(qx_n + n\varphi)$, respectively. Then, $\zeta_n(x_n)$ and $\delta\zeta_n(x_n)$ are related to $\zeta_m(x_m)$ and $\delta\zeta_m(x_m)$ by $\zeta_n(x_n) = \zeta_m(x_n + (n-m)\varphi/q)$ and $\delta\zeta_n(x_n) = \delta\zeta_m(x_n + (n-m)\varphi/q)$, respectively. Using these relationship, $\delta\mathcal{F}_{\text{el}}^{mn}/\delta\zeta_m$ is given by

$$\frac{\delta\mathcal{F}_{\text{el}}^{mn}}{\delta\zeta_m(s)} = -\frac{2(1-\sigma^2)P^2}{\pi E\ell^2(m-n)^2}\left\{\int_{-\infty}^{\infty}d\tilde{t}\left[\frac{-\tilde{t}^2 + 2}{[\tilde{t}^2+1]^{5/2}}\right.\right.$$

$$\times\{1 - \cos[(m-n)\varphi]\cos[q\ell(m-n)\tilde{t}]\}\Big]$$

$$+ \cos[(m-n)\varphi]q\ell(m-n)$$

$$\left.\left.\times\int_{-\infty}^{\infty}d\tilde{t}\left[\frac{\tilde{t}}{[\tilde{t}^2+1]^{3/2}}\sin[q\ell(m-n)\tilde{t}]\right]\right\}\zeta_m(s).$$

$$\text{(A6)}$$

Note that this operation is valid only for $q > 0$ and is not valid for $q = 0$. The contribution of the monopole-monopole interactions to the chemical potential of adatoms at the mth step, μ_m^{el}, is the summation of $\delta\mathcal{F}_{\text{el}}^{mn}/\delta\zeta_m$ in Eq. (A6) over n:

$$\mu_m^{\text{el}} = \sum_{\substack{n=-\infty \\ (n\neq m)}}^{\infty}\frac{\delta\mathcal{F}_{\text{el}}^{mn}}{\delta\zeta_m(x_m)}$$

$$= -\left[\frac{4(1-\sigma^2)P^2}{\pi E\ell^2}\sum_{\tilde{n}=1}^{\infty}\frac{Y(q\ell,\tilde{n},\varphi)}{\tilde{n}^2}\right]\zeta_m(x_m),\quad \text{(A7)}$$

where

$$Y(q\ell,\tilde{n},\varphi) = \int_{-\infty}^{\infty}dt\left[\frac{-t^2+2}{[t^2+1]^{5/2}}[1 - \cos(\tilde{n}\varphi)\cos(q\ell\tilde{n}t)]\right]$$

$$+ \cos(\tilde{n}\varphi)q\ell\tilde{n}\int_{-\infty}^{\infty}dt\frac{t\sin(q\ell\tilde{n}t)}{[t^2+1]^{3/2}}.\quad \text{(A8)}$$

The equilibrium concentration for a modulated step is determined by the chemical potential resulting from a step-line free energy and elastic interactions between the steps. The chemical potential due to a step-line free energy is given by $\gamma\kappa_m \sim \gamma q^2\zeta_m(x_m)$, where γ is a step-line free energy and κ_m is the local curvature of the mth step. Therefore, the chemical potential $\mu_m(x_m)$ is given by

$$\mu_m(x_m) = \left[q^2\gamma - \frac{4(1-\sigma^2)P^2}{\pi E\ell^2}\sum_{\tilde{n}=1}^{\infty}\frac{Y(q\ell,\tilde{n},\varphi)}{\tilde{n}^2}\right]\zeta_m(x_m).$$

$$\text{(A9)}$$

Consequently, the equilibrium concentration of the mth step, $c_{\text{eq}}^{h_m}$, in Eqs. (2.4) and (2.5), is given by

$$c_{\text{eq}}^{h_m} = c_{\text{eq}}^0 + \Gamma(q)\zeta_m(x)\quad \text{(A10)}$$

where

$$\Gamma(q) = \frac{\Omega c_{\text{eq}}^0\gamma}{k_B T}q^2 - \frac{\Omega c_{\text{eq}}^0}{k_B T}\frac{4(1-\sigma^2)P^2}{\pi E\ell^2}\sum_{\tilde{n}=1}^{\infty}\frac{Y(q\ell,\tilde{n},\varphi)}{\tilde{n}^2}.$$

$$\text{(A11)}$$

[1] M. Mundschau, E. Bauer, and W. Telieps, Surf. Sci. **213**, 381 (1989).

[2] J. M. Gaines, P. M. Petroff, H. Kroemer, R. J. Simes, R. S. Geels, and J. H. English, J. Vac. Sci. Technol. B **6**, 1378 (1988).

[3] J. E. Ortega, A. Mugarza, V. Repain, S. Rousset, V. Perez-Dieste, and A. Mascaraque, Phys. Rev. B **65**, 165413 (2002).

[4] M. Tanaka and H. Sakaki, Jpn. J. Appl. Phys., Part 2 **27**, L2025 (1988).

[5] J. Villain and A. Pimpinelli, *Physics of Crystal Growth* (Cambridge University Press, Cambridge, England, 1998).

[6] T. Maroutian, L. Douillard, and H. J. Ernst, Phys. Rev. Lett. **83**, 4353 (1999).

[7] T. Maroutian, L. Douillard, and H. J. Ernst, Phys. Rev. B **64**, 165401 (2001).

[8] N. Neel, T. Maroutian, L. Douillard, and H. J. Ernst, Phys. Rev. Lett. **91**, 226103 (2003).

[9] J. Tersoff and E. Pehlke, Phys. Rev. Lett. **68**, 816 (1992).

[10] R. M. Tromp and M. C. Reuter, Phys. Rev. Lett. **68**, 820 (1992).

[11] C. Alfonso, J. M. Bermond, J. C. Heyraud, and J. J. Metois, Surf. Sci. **262**, 371 (1992).

[12] A. Riposan, G. K. M. Martin, and J. M. Millunchick, Appl. Phys. Lett. **83**, 4518 (2003).

[13] W. K. Burton, N. Cabrera, and F. C. Frank, Philos. Trans. R. Soc. London, Ser. A **243**, 299 (1951).

[14] V. I. Marchenko and A. Y. Parshin, Sov. Phys. JETP **52**, 129 (1980).

[15] A. F. Andreev and Y. A. Kosevich, Sov. Phys. JETP **54**, 761 (1981).

[16] V. M. Kaganer and K. H. Ploog, Phys. Rev. B **64**, 205301 (2001).

[17] B. Houchmandzadeh and C. Misbah, J. Phys. I **5**, 685 (1995).

[18] S. Paulin, F. Gillet, O. Pierre-Louis, and C. Misbah, Phys. Rev. Lett. **86**, 5538 (2001).

[19] J. Tersoff and R. M. Tromp, Phys. Rev. Lett. **70**, 2782 (1993).

[20] J. Tersoff and F. K. LeGoues, Phys. Rev. Lett. **72**, 3570 (1994).

[21] J. Tersoff, Y. H. Phang, Z. Y. Zhang, and M. G. Lagally, Phys. Rev. Lett. **75**, 2730 (1995).

[22] J. Tersoff, Phys. Rev. Lett. **80**, 2018 (1998).

[23] F. Liu, J. Tersoff, and M. G. Lagally, Phys. Rev. Lett. **80**, 1268 (1998).

[24] F. Leonard and J. Tersoff, Appl. Phys. Lett. **83**, 72 (2003).

[25] P. Muller and A. Saul, Surf. Sci. Rep. **54**, 157 (2004).

[26] M. Schroeder and D. E. Wolf, Surf. Sci. **375**, 129 (1997).

[27] G. Ehrlich and F. G. Hudda, J. Chem. Phys. **44**, 1039 (1966).

[28] R. L. Schwoebel, J. Appl. Phys. **40**, 614 (1969).

[29] G. S. Bales and A. Zangwill, Phys. Rev. B **41**, 5500 (1990).

[30] Z. Hu, S. Li, and J. S. Lowengrub (unpublished).

[31] J. P. Bourdin, D. Wang, J. P. Lecoq, and X. N. Phu, Opt. Eng. **37**, 1268 (1998).

[32] E. M. Lifshitz and L. D. Landau, *Theory of Elasticity* (Butterworths-Heinemann, London, 1995).

[33] L. Proville, Phys. Rev. B **64**, 165406 (2001).

[34] D.-H. Yeon, P.-R. Cha, and J.-K. Yoon, Mater. Sci. Forum **426-4**, 3879 (2003).

[35] D.-H. Yeon, P.-R. Cha, S.-I. Chung, and J.-K. Yoon, Met. Mater. Int. **9**, 67 (2003).

[36] P. W. Voorhees, G. B. Mcfadden, and W. C. Johnson, Acta Metall. Mater. **40**, 2979 (1992).

[37] J. P. Hirth and J. Lothe, *Theory of Dislocation* (John Wiley, New York, 1982).

[38] N. C. Bartelt, R. M. Tromp, and E. D. Williams, Phys. Rev. Lett. **73**, 1656 (1994).

[39] W. Hong, H. N. Lee, M. Yoon, H. M. Christen, D. H. Lowndes, Z. Suo, and Z. Zhang, Phys. Rev. Lett. **95**, 095501 (2005).

[40] A. J. Bray, Adv. Phys. **51**, 481 (2002).